Airborne GNSS-R: A Key Enabling Technology for Environmental Monitoring

Adrian Perez-Portero [ID], Joan Francesc Munoz-Martin [ID], *Student Member, IEEE*,
Hyuk Park [ID], *Senior Member, IEEE*, and Adriano Camps [ID], *Fellow, IEEE*

Abstract—Weather forecast using GNSS-R relies, to a large extent, on data acquired by airborne and spaceborne platforms due to the extended coverage that can be achieved. GEO satellites can retrieve measurements over large areas but with spatial resolutions on the order of thousands of meters per pixel. LEO satellites with polar orbits can provide measurements over the entire world, but they cannot provide good spatial or high temporal resolutions by themselves. LEO constellations of small satellites have the same coverage with improved spatial resolution and revisit times by using data fusion techniques. High-altitude pseudo-satellites offer an excellent temporal and spatial resolution but only over limited areas. In this article, the potential of using hosted GNSS-R payloads on commercial aircraft is explored as an alternative and cost-effective means to achieve a very high resolution and a very low revisit time for regional environmental applications. Finally, a case study of soil moisture monitoring over Europe is presented, including an analysis of the expected performance.

Index Terms—Airborne instruments, Earth observation, GNSS-R, soil moisture, weather nowcasting.

I. INTRODUCTION

G NSS-R [1] is a growing remote sensing technique, and its applications have been proven from ground-based equipment, airborne instruments, and also satellites. Ground-based instruments have been broadly used to develop and validate models, technologies, and also to provide periodic measurements over the same area. However, these types of sensors lack the versatility of mobile ones, such as the capability to take measurements from different areas.

This technology has been proven to work in five space-based missions: U.K.-DMC [2], TDS-1 [3], [4], CYGNSS [5]–[7],

BF-1 [8], and, more recently, FSSCat [9]. The former was only a proof-of-concept mission that demonstrated the capabilities and potential of GNSS-R from space, whereas TDS-1 and CYGNSS have provided a wealth of GNSS-R data that has been successfully used for sea state retrieval [4], sea ice detection [10], soil moisture [11]–[13], target detection [14], [15], and waste on the ocean surface, among others.

Despite the fact that GNSS-R systems have already been deployed in spaceborne platforms, airborne-based GNSS-R can provide better observations than in the spaceborne case, with improved spatial resolution [16] and much better revisit time over the flight routes. In the case of specular reflections, which usually happen over land and ice, the spatial resolution of the sensor is significantly improved as the reflection is determined by the size of the first Fresnel zone [17]–[19]. This size (l_{Fr}) depends on the instrument altitude as $l_{Fr} = \sqrt{\lambda h}$ [1], where λ is the wavelength of the GNSS signal, h is the height of the receiver, and the incidence angle is assumed to be 0. This area is in the order of 45 m for an airplane flying at a 10-km height, or for a spacecraft orbiting at a height of 500 km, it would be in the order of 300 m. In combination with the newest GNSS signals, such as the GPS L5 band, new applications can be developed such as swell monitoring [20]–[22]. The extensive applications of GNSS-R possible at lower heights, the reduced power, cost, and volume budgets needed aboard airplanes compared to spacecrafts, and the improved revisit time for remote areas due to the large number of commercial airplanes have sparked interest in the implementation of the airborne GNSS-R technique.

This work was initiated in preparation for an ESA Invitation to tender published in May 2019 (EXPRO+ NAVISP-EL1-028: GNSS SCIENCE WITH COMMERCIAL AIRCRAFT, ESA Open Invitation to Tender AO9877, Opening Date: May 24, 2019, Closing Date: July 19, 2019 13:00:00). In this work, a review of some possible applications of GNSS-R techniques enabled by airborne instruments is first presented. Then, the capability to perform soil moisture is explored in detail, with a discussion on the processing necessary to acquire meaningful measurements. Afterwards, the results of a simulation using real plane data obtained from a network of ADS-B receivers is used to calculate the locations of the specular reflection points, with special focus over Europe.

II. STATE-OF-THE-ART

To understand the climate change impact, the United Nations established in 1992 the Global Climate Observing System.
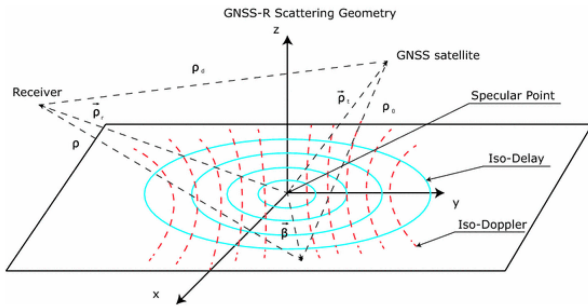
Fig. 1. Geometry of the reflection of a GNSS signal over the sea, providing the basis to perform GNSS-reflectometry.

Through this organization, up to 54 essential climate variables (ECVs) were defined, focusing on particular aspects of our planet. ECV monitoring is imperative to understand climate trends and to mitigate and predict the effects of global warming, and some of them can be observed through the use of GNSS-R. GNSS-R represents a very interesting use of opportunistic signals (GNSS) as the transmitter part of a multistatic radar. The main product of GNSS-R is the delay-Doppler map (DDM) of the scattered signal. From it, multiple physical parameters can be extracted, taking into account the properties of the signal prior to the reflection, and the effects of the scattering surface at the GNSS band (Fig. 1). The reflection coefficient of the GNSS signal on a surface is given by

$$\Gamma_{\text{RE,eff}} = |\rho_{\text{RL}}|^2 e^{-4k^2\sigma_h^2\cos^2\theta_i} \tag{1}$$

where $\Gamma_{\text{RE,eff}}$ is the reflectivity, ρ_{RL} is the Fresnel reflection coefficient (RHCP to LHCP), $k = 2\pi/\lambda$ is the wavenumber, λ is the electromagnetic wavelength, σ_h denotes the surface rms height, and θ_i is the incidence angle. From (1), it can be seen how the incidence angle has a strong effect on the attenuation introduced in the reflectivity, limiting the satellites from which the obtained GNSS-R measurements are accurate.

From the reflectivity of the surface and other physical parameters extracted from the DDM, several ECVs can be obtained, but GNSS-R can also be used for other applications. In the following sections, some of the main applications of GNSS-R that may significantly benefit from airborne GNSS-R instruments will be described as well as their requirements.

A. Sea State Information

Monitoring sea state is one of the first applications that were envisaged for GNSS-R [22], [23]. Surface wind, swell, and pollution conditions are some of the measurements usually obtained over sea, which could be potentially sensed with varying degrees of resolution depending on the GNSS signal used and the receiver height.

Previous ground-based and airborne GNSS-R campaigns have showcased the potential applications of this technique. In [24], an extensive data set of GNSS-R acquisitions was used to attempt oceanic measurements (altimetry and scatterometry), soil moisture sensing, and sea ice and snow characterization. In [22], GPS L5 signals (which offer a spatial resolution of 30 m as compared to the 300 m of the GPS L1 C/A code signals) are used to measure swell over the sea, when the swell wavelength is comparable or larger than the width of the GNSS signal auto-correlation function.

From space, multiple missions have provided GNSS-R data over seas and, thus, contributed to sea state retrieval. In [25], sea surface altimetry is obtained using GNSS-R measurements from the CYGNSS mission. In [4], ocean winds were estimated with data from the TDS-1 mission. Another remarkable example of the potential application of GNSS-R for sea state determination is the detection of tsunamis using wave altimetry measurements, which was analyzed in detail in [26]. In [27], different approaches using GNSS-R are used also in the detection of tsunamis.

Estimation of the sea state is key in weather prediction, estimation of sea currents, studying marine wildlife, optimizing merchant routes for ships, and much more. In the case of navigation, if sea state and ice presence could be estimated prior to departure, alternative routes could be used for significant time and cost savings. For example, ships traveling from economic poles such as Northern Europe and East Asia could travel through the Arctic North route (if clear), reducing the distance covered by ships by up to 3000 nautical miles [28].

Thus, having improved revisit times and coverage can benefit all the aforementioned use cases, and airborne GNSS-R can play a key role in this endeavor.

B. Soil Moisture

Vegetation health is closely linked to the water content found in the soil, where plants thrive. Thus, low soil moisture values indicate a hydric stress and potential danger for the vegetation. On the other hand, moderate or high values can foster floods, as water cannot be absorbed, or erosion [29]. Periodic measurements of soil moisture are being used nowadays for controlling the irrigation of crops, to estimate the risk of forest fires by monitoring dry forest areas, and, overall, to have more information on the water cycle.

Soil moisture significantly benefits from the use of airborne GNSS-R instruments [30]. High revisit times over agricultural and forest areas can lead to improved efficiency in agriculture, forest fire prediction, and assessments of lost biomass after wildfires. There are several techniques to monitor soil moisture: *in situ* probes, L-Band microwave radiometry [31], [32], thermal infrared spectrometers, radar, scatterometers [33], synthetic aperture radars (SARs) [34]–[36], and GNSS-reflectometry [13], [37].

GNSS-R has been shown to offer enhanced spatial resolution (300 m from space and 40 m from transatlantic airplanes) by averaging multiple measurements into bins [30] or averaging in space and performing time-series analysis [7].

A tradeoff between spatial resolution and radiometric resolution can be seen in the aforementioned works in a way that it is not possible to achieve a good radiometric and spatial resolution at the same time. In [30] and [38], the soil moisture error was reduced considerably when averaging more than 25 samples, and the smaller the number the averages, the larger the error; thus, a worse radiometric resolution can be achieved.

As a considerable amount of measurements over a single bin are needed to obtain accurate soil moisture measurements, airborne GNSS-R emerges as a good solution over land, where planes can provide measurements almost continuously.

C. Target Detection

Objects on the Earth's surface that are susceptible to being detected using GNSS-R instruments include sea ice [39], man-made objects on the sea surface [14], [15], oil slicks [40], etc. Their detection is based on the difference of the reflection coefficient between the sea around it and the target. Signals that reflect on ice, for example, have a much higher reflectivity, which translates to different features in DDMs [10].

In [41], an assessment of the sensitivity of different GNSS signals is presented, concluding that even though GALILEO signals achieve lower SNR than GPS ones, they provide an improved surface resolution. This can be directly translated to target detection of smaller objects than with GPS signals.

The major constraint for this technique in its use for sea traffic control is the revisit time. In [14], it can be seen that with a constellation of up to 32 satellite-based GNSS-R instruments, a best case revisit time of 2 h could be achieved. Using airborne GNSS-R instruments, a higher revisit time over the flight routes can be expected, as it will be seen in Section IV-E.

D. Ocean Plastic Waste

Plastic that is not properly disposed often finds its way to oceans. Due to the ocean currents, most plastic ends up floating in the so-called garbage patches. One of the most notable examples is the Great Pacific garbage patch, a gyre of marine debris located roughly from 135°W to 155°W and 35°N to 42°N [42]. The eastern part of this patch is located between Hawaii and California, whereas the western part extends from Japan to the Hawaiian Islands.

In most places, the typically low density of the plastics in this patch (four particles per cubic meter) prevents detection by satellite imagery, but it is thought that detection of plastic concentration could be achieved from airborne GNSS-R instruments possibly because of a change in the surface roughness, a phenomenon that is increased by the presence of surfactants.

When plastics accumulate on a single spot, as is the case with the Great Pacific garbage patch, wind-driven high-frequency waves could get damped by the presence of plastics. This change in the waves could possibly get detected with GNSS-R. Another option is that when large amounts of plastic are near the surface, it could even change the reflection coefficient itself and, thus, detectable also with GNSS-R. As there are numerous flight routes linking Japan, Hawaii, and California, planes flying over them could be used to track the size or composition of these garbage patches.

III. METHODOLOGY

In order to characterize the performance of a GNSS-R mission, there are three main parameters that need to be studied: coverage, spatial resolution, and temporal resolution. Coverage refers to the surface that can be monitored with the instrument, taking into account its swath and movement. Spatial resolution directly links the observable with the minimum area from which the measurement can be obtained, resulting in better spatial resolution the smaller the area is. Temporal resolution is the periodicity at which measurements are obtained over the same area, with better temporal resolution resulting from very frequent repetition. Airborne GNSS-R missions have the potential to provide excellent temporal resolution due to the amount of aircraft that are in flight at any given moment, spatial resolution thanks to their reduced height compared to other platforms, and coverage over most inhabited land. To provide an indicator of the performance of the proposed network of airborne GNSS-R instruments, a simulation using real data was performed.

A. Simulation

Plane positions for all commercial aircraft with ADS-B activated were obtained from a large-scale ADS-B sensor network [43] between September 17, 2019 and April 17, 2020 to simulate the results that could be achieved if every single plane was equipped with a GNSS-R instrument. The data was stored in a relational database to allow further analysis such as filtering by aircraft model or airlines, but to illustrate the full potential, it is assumed that all aircrafts are equipped with a GNSS-R instrument. To obtain the swath of each instrument, the GPS constellation is used to find all the specular reflection points used for GNSS-R observables.

Positioning data was obtained every 10 s, and the specular points were calculated in real time prior to storage in the database. To perform the specular point calculation, the GPS satellites' positions were calculated using data downloaded from NASA's Crustal Dynamics Data Information System [44]. The ephemeris and almanac of all GPS satellites at any point in time can be obtained by propagating the two-line elements using the SGP4 [45] model. By using the timestamp of the aircraft's positions, the position of GPS satellites at that point in time can also be obtained, allowing for a very accurate simulation.

Using the same procedure as described in [46], the specular reflection point of the GPS signals is obtained [47] by an iterative algorithm which uses the WGS84 ellipsoid and the positions of the transmitter and receiver. For each airborne receiver, a number of specular points corresponding to the GPS satellites in view at that moment in time were calculated. To avoid specular points with poor elevations, a mask was set to 20° of elevation (1) according to data obtained from previous missions and studies [48], as a compromise between signals of opportunity that would be acquired and the quality of the measurements. Thus, for each plane in the world and every 10-s window during months of data, 5–12 specular points (belonging to the different GPS satellites in view) were calculated with a precision under 10 m. This procedure can be seen in Fig. 2.

B. Coverage and Temporal Resolution

Obtaining the performance of the network in terms of coverage and temporal resolution implies calculating the percentage
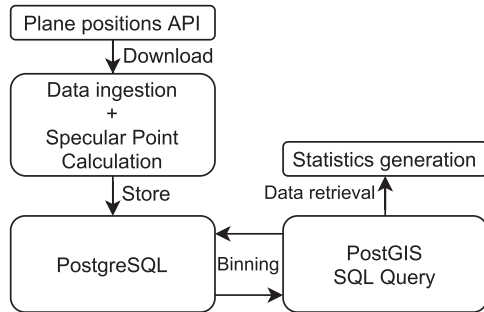
Fig. 2. Block diagram of the processing chain.

Fig. 3. Spread of the specular points received by an airplane taking off from the Dubai International Airport, depending on its height.

of land that is covered by GNSS-R observables and the frequency at which these measurements are repeated over the same area. To ease the calculation of relevant statistics and maps, all specular points were binned into differently sized hexagonal grids, depending on the area covered by the case study:

1) a coarse 100×100 km worldwide grid was used to obtain information regarding global coverage;
2) a 36×36 km grid over land to obtain global land coverage for soil moisture;
3) a 9×9 km grid over the European Union including the U.K. to perform a more precise study also for soil moisture;
4) a 9×9 km grid over the Mediterranean Sea for sea state information, target detection, and waste detection study.

The hexagonal grids were calculated using the WGS 84/NSIDC EASE-Grid 2.0 Global projection [49], standard in remote sensing products, and for visualization purposes, Geographical Information System software was used to plot the specular points as well the differently sized bins.

C. Spatial Resolution

The spatial resolution of a GNSS-R instrument is given by the size of the first Fresnel zone, which can be calculated as follows:

$$Fz = \frac{\sqrt{\frac{\lambda \cdot h}{\cos \theta_{\text{inc}}}}}{\cos \theta_{\text{inc}}} \qquad (2)$$

where λ is the wavelength of the signal, h is the height of the receiver, and θ_{inc} is the incidence angle at which the signal is received. If the instrument has as many channels for GPS reception as satellites can be in view, it is possible to track up to eight different GPS transmitters at the same time. This also means that there can be eight specular points covering different areas simultaneously.

Due to the geometry of the GNSS reflection and the difference in heights of the transmitter and receiver, the spread of the specular points changes with the height of the plane as well as with the movement of the GPS satellites. In Fig. 3, the trajectory of a plane taking off from the Dubai International Airport can be seen and the specular points can be calculated.

The plane is color coded depending on its height, whereas the specular points are colored depending on the GPS satellite that is providing the signal. As the plane flies higher, the area
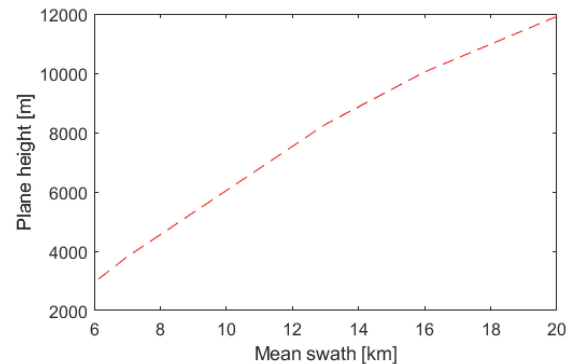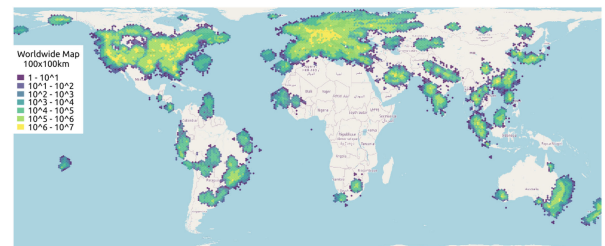

Fig. 4. Mean specular point spread depending on the plane height, which corresponds to the swath of the instrument.

Fig. 5. Worldwide density map over a five-day period, with 100×100 km hexagonal bins, showing the limitations of ADS-B receivers.

covered by the specular points becomes wider, and the position of the specular point from SV26 changes relative to the plane due to the movement of the satellite. The relationship between the height of the plane and the maximum size of the specular points is shown in Fig. 4. This results in planes flying at cruise altitudes covering larger areas than those flying local routes.

IV. SIMULATION RESULTS

Due to limitations of the ADS-B receivers used by the data provider, no information from the planes is collected while they are out of range from the network, which corresponds to the period when the planes are flying over the ocean (Fig. 5). From this limitation, this work focuses on soil moisture measurements over land and waste and target detection over the Mediterranean Sea.

A. World

The theoretical coverage that could be achieved by a fleet of airborne GNSS-R is, in all cases, lower than that of an Earth Observation satellite in a polar orbit, especially over the oceans. Even then, the coverage achieved by airborne receivers could be enough to satisfy specific cases which might need better revisit times than those provided by the satellites.

In Fig. 5, the cumulative specular points over a five-day period, binned in 100×100 km hexagonal bins, can be found. From this figure, the maximum reach of the ADS-B receivers of the data provider used can be obtained, which would allow applications such as coastal GNSS-R but not sea state determination. It is important to note that most of the areas over land not shown in the density map do have planes flying over them, but as no ADS-B receivers from the used data provider are in range, no information was reported.

With the current data, only 13.52% (using the 100×100 km grid) of the world could be mapped by airborne GNSS-R, including the ocean and the poles. By connecting the areas with specular points, a more realistic density map could be obtained, covering a higher percentage of the world. To obtain a better estimate of land coverage for soil moisture applications, a 36×36 km hexagonal grid over land was used, with results indicating that up to 25% of land could be measured. It is clear from Fig. 5 that a higher percentage of land is covered by planes, but more accurate data is required to obtain this number.

B. South America

The Amazon rainforest represents over half of the planet's remaining rainforests and comprises the largest and most biodiverse tropical rainforest in the world. The Amazon rainforest encompasses $5\,500\,000$ km^2, and, by 2018, 17% was already destroyed, with the fires in 2019 aggravating the situation.

Amazonian evergreen forests account for about 10% of the world's terrestrial primary productivity and 10% of the carbon stores in ecosystems. For this reason, it is of utmost importance to monitor the biomass and health of the Amazon rainforest to avoid further loss, helping to restore it to combat climate change. The Amazonian rainforest is an important target to monitor by itself, including ECVs regarding the biosphere and hydrosphere.

A detailed case study for the area surrounding the Amazonian rainforest was conducted, using the 36×36 hexagonal grid over land. In Fig. 6, even though no information on the planes overflying the Amazon rainforest was collected, it can clearly be seen how the routes that connect the nodes seen in the figure can provide an almost complete coverage of the Amazon rainforest. Thanks to the short length of the local flights in South America, weather nowcasting of ECVs and the state of the forest would be possible, with a strong emphasis on fire prevention and soil moisture monitoring of deforested regions.

C. Australia

Eastern Australia is one of the most fire-prone regions of the world. From September 2019 until March 2020, at the same time that the data for this simulation was taken, Eastern Australia
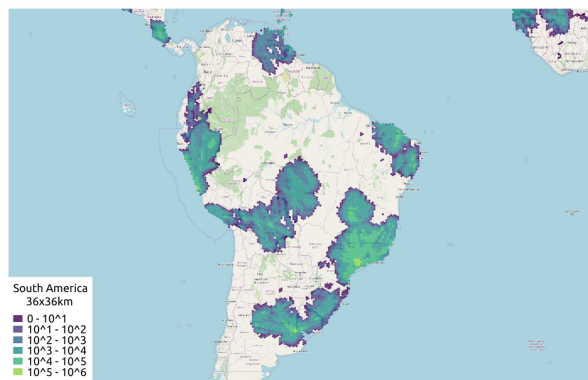

Fig. 6. South America density map on a 36×36 km grid over a five-day period.
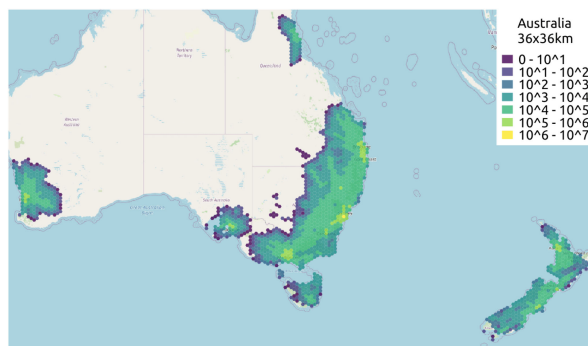

Fig. 7. Australia density map on a 36×36 km grid over a five-day period.

suffered one of the worst bush fires in history, also contributing to 2019 being one of the hottest years for Australia. Fires caused massive property and personal damages, and the east coast's forests suffered massive destruction. For this reason, it is very important to monitor soil moisture with good revisit times to predict bushfires before they happen and to act quickly if they do.

Fig. 7 shows the coverage obtained by the simulation, with the entirety of the east coast covered by measurements with excellent temporal resolution, mainly due to the short flights and very close population centers found in Australia.

The main measurement over this area would be soil moisture, which would allow for monitoring of forest fires, vegetation height, or above-ground biomass [50] with excellent revisit time, allowing for rapid responses to any event that could endanger civilians or the forest.

Thanks to the flight routes between Australia, Tasmania, and New Zealand, an excellent coverage of the Tasmanian Sea can be achieved. This would allow for a monitoring and early-response network to predict tsunamis using sea state determination from GNSS-R instruments. Recent examples of tsunamis in the Tasmanian Sea, such as the one occurred in March, 2011, reveal that with continuous monitoring of the sea state, extensive precautions can be undertaken, potentially saving the lives and material properties of thousands.

Eastern Australia also houses the OzNet hydrological monitoring network, near the town of Yanco, New South Wales. This site contains 37 soil moisture stations distributed over a
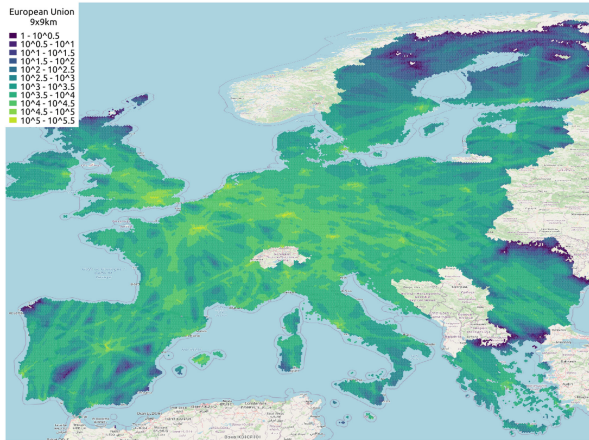
Fig. 8. Europe density map with a 9×9 km grid over a five-day period.

Fig. 9. Coverage of European Union land by airborne GNSS-R in a day, per hour, using a 9×9 km hexagonal grid.

Fig. 10. Average number of specular points per bin in Europe, depending on the hour of the day, using a 9×9 km hexagonal grid.

60×60 km area, and it is commonly used for calibration of L-band microwave radiometers that attempt soil moisture remote sensing. Further data for calibration could be provided by airborne GNSS-R over the same area, allowing to cross-check and validate with other GNSS-R instruments, increasing the accuracy of the measurements.

D. European Union

A more exhaustive study was performed over the European Union, with a 9×9 km grid and hourly aggregates. Fig. 8 shows the five-day cumulative specular point count, binned in 9×9 km hexagonal bins. It can be observed that the routes connecting main European cities such as Madrid, Paris, and Munich have a higher concentration of specular points, reaching 300 000 specular points per bin, which could be translated to over 40 specular points per cell and per minute.

Remote areas in the North of Finland, by contrast, hardly reach a few hundred specular points, similar to the north-western coast of Spain, where not many planes fly over, as there is no direct route between major cities crossing that area.

In northern Europe, for instance, higher temperatures due to climate change have increased snowmelt and liquid precipitation [51]. Biomass and vegetation are growing in places that historically had been covered in snow, and, thus, new biomes could be emerging. Using airborne GNSS-R, this area could be monitored to assess changes in biomass and sea-ice. This is of utmost importance because upcoming missions such as ESA BIOMASS P-band SAR will not be operational in the boreal forests of the Northern hemisphere [52].

Overall, the land coverage over European Union countries is excellent, taking into account the improved revisit time as compared to satellite instruments. In Fig. 9, the total land coverage over the European Union, per hour of the day can be seen. A mean coverage of 74.68% is achieved during the entire day, with a maximum of 87% during the peak hours of the day.

Most measurements occur over the same paths, as seen in Fig. 10, where the average number of specular points per bin depending on the hour of the day, with time represented in CET, is shown. As there is a great variance in the amount of specular
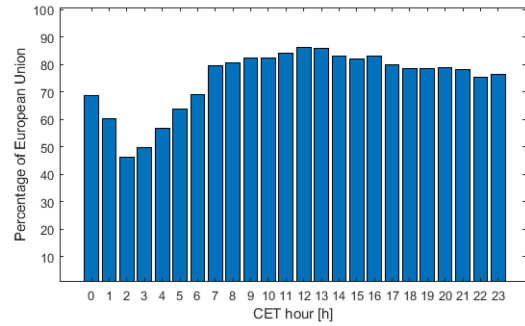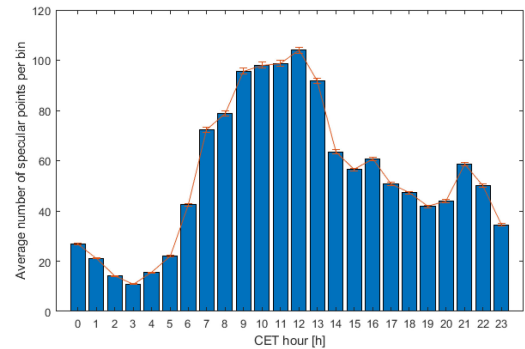
points per bin, depending on whether the cells are below popular flight paths or not, to indicate the uncertainty around the estimate of the mean measurement, we use the standard error of the mean calculated as the standard deviation divided by the square root of the number of observations. It has then been converted to 95% confidence intervals by multiplying it by the inverse value of the *t*-distribution with a given probability and degrees of freedom (observations).

During the peak hours of the day, far more specular points are happening per bin than in the afternoon, whereas the land coverage remains very similar throughout the mid-end of the day. This indicates that during peak hours, revisit time increases dramatically over covered areas. Averaging the specular count for all the hours of the day, we obtain an average count per bin and hour of 48.98 ($\sigma = 66.31$) specular points, with a median of 31.63. This average translates to ~8 specular points every 10 min all over Europe, which would enable for incredibly complex acquisition strategies that rely on almost-instantaneous data.

E. Mediterranean Sea

The Mediterranean Sea is a very interesting target for sea traffic control, sea state information, and plastic garbage detection. Averaging the specular count for the five days chosen, we obtain an average count per bin and hour of 15.84 ($\sigma = 26.41$) specular points, with a median of 7.96. A total coverage of 75.63% is achieved, as seen in Fig. 11.
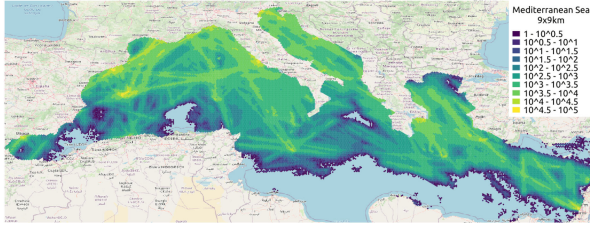
Fig. 11. Mediterranean Sea density map using a 9×9 km grid over a five-day period.

A revisit time of ~16 reflections per hour in a single bin could very well comply with the requirements of sea traffic control, depending on the implementation of the search algorithm. For sea state information, the extensive coverage and good revisit time could enable weather nowcasting to facilitate maritime routes.

V. DISCUSSION

A. Performance of the Network

The coverage and revisit time presented in the previous section ensures that measurements of soil moisture over Europe can be obtained continuously. In order to extract accurate soil moisture estimates, it is important to average the different observables that occur over the same areas. In the CYGNSS Soil Moisture retrieval, this is done by binning reflectivity values calculated for each specular point acquisition over an EASE-grid at 36×36 km resolution [6].

The number of points that are needed to be averaged to obtain accurate measurements are linked to the size of the Fresnel Zone (2). For the airborne case, Fz will range between 70 and 120 meters of diameter, depending on the different parameters. If binning the measurements in 9×9 km grids, in order to obtain the most accurate results (i.e., to statistically cover the whole area with reflections), we would need a number of points equivalent to the ratio between the areas, e.g., 90 points.

In [30], the relationship between the sample number of CYGNSS observables within each bin and its direct impact on the accuracy of soil moisture measurements is explained. Furthermore, in [53], a study of the SM retrieval algorithm from an airborne platform is presented. The relationship of the evolution of the RMSE using the number of GNSS-R observables with respect to the SM ground truth from the SMOS mission is obtained and then extrapolated to the results presented in this work to characterize the accuracy of the measurement with respect to the repeated observables over the same bin. The more observables being averaged together, the lower the error with respect to the ground truth. By extrapolating the results obtained in [53, Fig. 15] and assuming that the same algorithm for SM retrieval is used, we obtain Fig. 12, where the RMSE of the SM measurements is related to the number of GNSS-R observables per bin, approaching a minimum around 90 (i.e., the whole bin is covered by observables).

In Fig. 13, we can see the different areas in Europe depending on the RMSE value obtained from Fig. 12, which translates to the different levels of precision for SM estimation. In this
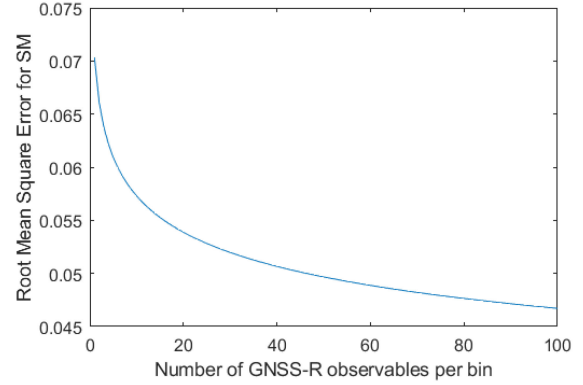

Fig. 12. Relationship between the number of GNSS-R observables per bin and the RMSE of soil moisture measurements.
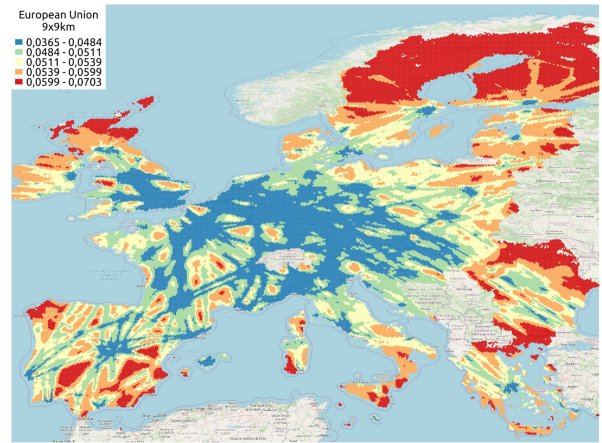

Fig. 13. Estimated RMSE for soil moisture estimation, using the hourly average of measurements per bin. In light blue, very low RMSE values are found, with low revisit times (see color bar in the figure indicating the RMSE values).

simulation, which performs GNSS-R measurements every 10 s (with the same frequency as the position updates from ADS-B), areas with a high affluence of planes commonly surpass 90 observables per bin. On the other hand, in remote areas, it is very difficult to achieve those values. In order to solve this problem, the rate at which acquisitions are performed needs to be tuned depending on the area the plane is overflying: In areas where the average number of points per bin is 9, for example, if the instrument performed measurements every second (i.e., 10 times more), 90 samples per bin could be obtained.

As mentioned before, revisit time is one of the main advantages of airborne GNSS-R when compared to spaceborne instruments. It is important to note that this improved revisit time mainly considers coverage over land, as airplanes are bound to fly from one airport to the other in almost straight lines. Less-common flight routes provide sparse coverage over remote areas, whereas commercial routes between main airports provide very frequent revisit times.

Being in the middle of multiple popular flight tracks, the Mediterranean Sea has been found to have excellent coverage and temporal resolution by commercial airlines and could be used in the future for test flights to evaluate the goodness of the

proposed approach. Using regional flights, sea state determination, target, and even plastic waste detection could be obtained.

B. Comparison to CubeSat Receivers

CubeSat platforms are well suited for passive remote sensing due to the low power required for the instrument, the low cost of development and launch, and the large coverage. By contrast, airborne-mounted GNSS-R instruments are making use of already-existing planes, thus working on platforms of opportunity. Due to being constrained to existing flight routes, truly global coverage is not achieved with airplanes, but the improved revisit time can make it an optimal solution for regional applications that are constantly overflown by planes.

In terms of cost, massively produced GNSS-R receivers for airborne applications ($\sim$\$100) are orders of magnitude cheaper than a 1-unit CubeSat equipped with a GNSS-R instrument such as ^{3}Cat-4 ($\sim$\$100 000), even without taking into account the cost of launch, operations, and personnel.

Data retrieval is especially advantageous for the case of the airborne instruments, as data could be received either in real time by using satellite communication constellations providing Internet access over the oceans or downloaded at the end of the flight once the plane has arrived at the destination airport, using other means of wireless connection. In the CubeSat case, this retrieval would need to be performed with predetermined ground stations over several passes every day, with expensive operation costs, and with more time elapsed until data can be accessed.

The effect of topography is also very different when comparing airborne to spaceborne receivers [48], [54]. The specular reflection corresponds to scattering processes in which waves from a single direction are reflected into a single reflected direction. On the opposite side, in diffuse scattering, the incoming waves are reflected in a broad range of directions. The specular-to-diffuse regime is determined by the roughness structures of the surface topography, rather than its dielectric properties. The first Fresnel zone described in this article, which corresponds to the area from which reflections are received, becomes larger as the height of the instrument increases.

For this reason, at higher altitudes, this area has a higher probability to contain distinct surface heights, and, therefore, the ratio of the coherent to incoherent component decreases (e.g., from 3% from a few hundred meters to 0.08% from a LEO) [55].

For soil moisture purposes, one of the most important metrics is the signal-to-noise ratio of the peak of the DDM. Since, at lower heights, the ratio coherent-to-incoherent component is larger, so is the power of the reflected signal, and the SNR.

C. Radio-Frequency Interference

As with every passive remote sensing method, RFI is a very real threat to GNSS-R sensors. Previous studies regarding RFI effects on GNSS-R measurements [56], [57] conclude that precorrelation and postcorrelation methods need to be implemented for RFI detection and mitigation in the receiver in order to retrieve accurate measurements. The use of a test bed [46] to characterize the effect of RFI on the GNSS-R instrument and to develop countermeasures is increasingly important before and during campaigns, as the problem of RFI remains unsolved and is continuously affecting active missions with passive sensors [58], [59].

Regarding the strong effects that RFI can have on the measurements, a compromise has to be made regarding the complexity and cost of the tentative GNSS-R receivers that would be mounted on airplanes: Either RFI contaminated samples are discarded upon detection with the consequent loss of information, but a cheaper system is built as a result, or mitigation techniques are used to recover as much data as possible at the expense of a costlier receiver. In the case of a theoretical worldwide network of airplanes, with the number of samples that would be generated, it might be better from the cost perspective to discard contaminated samples and recover the measurements from another airplane when the RFI disappears. A lower cost barrier of entry would be beneficial in the long run, while often-contaminated flight paths could be individually monitored to evaluate if RFI mitigation techniques could be implemented in a case-by-case basis.

VI. CONCLUSION

Several key areas that involve the main applications of GNSS-reflectometry have been presented and analyzed under the hypothesis of a fleet of airborne GNSS-R instruments, showcasing the benefits of this deployment in multiple fields. The performance of airborne GNSS-R has been explored through the coverage, spatial resolution, and temporal resolution that could be achieved by this technology. It was found that over most continental territories and especially over densely populated areas, airborne GNSS-R excels in the three performance indicators, thus becoming a very interesting technology to explore in the near future. Even over the ocean, long-haul flights may be able to provide valuable measurements that could revolutionize sea routes and monitor garbage patches or wind speed [60] and direction [61].

The theoretical soil moisture measurements that could be achieved by this system have been analyzed, and the coverage, temporal resolution, and RMSE presented make airborne GNSS-R a very competitive alternative to satellite-based GNSS-R missions. Using the system presented in this work with inter-European flights, very accurate soil moisture measurements could be obtained over a large area, providing valuable data for environmental monitoring and cross-validation of other instruments.

Advances in GNSS-R are happening rapidly, and many instruments are being developed with innovative technologies that could pave the way to a network of airborne GNSS-R. ESA proposed an Invitation to Tender to study this technology for remote sensing purposes in 2019, and projects such as [62] appeared with the objective to test this technology with real-world data from Air New Zealand's flights. The idea of ubiquitous airborne GNSS-R is becoming a reality, and some companies are starting to investigate airborne GNSS-R for remote sensing purposes due to the low cost and benefits that this technique can provide.

References

[1] V. U. Zavorotny, S. Gleason, E. Cardellach, and A. Camps, "Tutorial on remote sensing using GNSS bistatic radar of opportunity," *IEEE Geosci. Remote Sens. Mag.*, vol. 2, no. 4, pp. 8–45, Dec. 2014.

[2] M. Clarizia, C. Gommenginger, S. Gleason, C. Galdi, and M. Unwin, "Global navigation satellite system-reflectometry (GNSS-R) from the U.K.-DMC satellite for remote sensing of the ocean surface," in *Proc. IGARSS IEEE Int. Geosci. Remote Sens. Symp.*, 2008, pp. I-276–I-279.

[3] A. Camps, M. Vall·llossera, H. Park, G. Portal, and L. Rossato, "Sensitivity of TDS-1 GNSS-R reflectivity to soil moisture: Global and regional differences and impact of different spatial scales," *Remote Sens.*, vol. 10, Nov. 2018, Art. no. 1856.

[4] G. Foti *et al.*, "Spaceborne GNSS reflectometry for ocean winds: First results from the U.K. TechDemoSat-1 mission," *Geophys. Res. Lett.*, vol. 42, pp. 5435–5441, Jul. 2015.

[5] C. Ruf *et al.*, "CYGNSS: Enabling the future of hurricane prediction," *IEEE Geosci. Remote Sens. Mag.*, vol. 1, no. 2, pp. 52–67, Jun. 2013.

[6] M. P. Clarizia *et al.*, "Analysis of CYGNSS data for soil moisture retrieval," *IEEE J. Sel. Top. Appl. Earth Obs. Remote Sens.*, vol. 12, no. 7, pp. 2227–2235, Jul. 2019.

[7] M. M. Al-Khaldi, J. T. Johnson, A. J. O'Brien, A. Balenzano, and F. Mattia, "Time-series retrieval of soil moisture using CYGNSS," *IEEE Trans. Geosci. Remote Sens.*, vol. 57, no. 7, pp. 4322–4331, Jul. 2019.

[8] C. Jing, X. Niu, C. Duan, F. Lu, G. Di, and X. Yang, "Sea surface wind speed retrieval from the first Chinese GNSS-R mission: Technique and preliminary results," *Remote Sens.*, vol. 11, Dec. 2019, Art. no. 3013.

[9] J. F. Munoz-Martin *et al.*, "In-orbit validation of the FMPL-2 instrument - The GNSS-R and L-band microwave radiometer payload of the FSSCat mission," *Remote Sens.*, vol. 13, no. 1, 2021, Art. no. 121.

[10] A. Alonso-Arroyo, V. Zavorotny, and A. Camps, "Sea ice detection using U.K. TDS-1 GNSS-R data," *IEEE Trans. Geosci. Remote Sens.*, vol. 55, no. 9, pp. 4989–5001, Sep. 2017.

[11] N. Rodriguez-Alvarez *et al.*, "Soil moisture retrieval using GNSS-R techniques: Experimental results over a bare soil field," *IEEE Trans. Geosci. Remote Sens.*, vol. 47, no. 11, pp. 3616–3624, Nov. 2009.

[12] A. Camps *et al.*, "Sensitivity of GNSS-R spaceborne observations to soil moisture and vegetation," *IEEE J. Sel. Top. Appl. Earth Obs. Remote Sens.*, vol. 9, no. 10, pp. 4730–4742, Oct. 2016.

[13] C. Chew and E. Small, "Description of the UCAR/CU soil moisture product," *Remote Sens.*, vol. 12, May 2020, Art. no. 1558.

[14] A. Di Simone, H. Park, D. Riccio, and A. Camps, "Sea target detection using spaceborne GNSS-R delay-doppler maps: Theory and experimental proof of concept using TDS-1 data," *IEEE J. Sel. Top. Appl. Earth Obs. Remote Sens.*, vol. 10, no. 9, pp. 4237–4255, Sep. 2017.

[15] C. Hu, C. Benson, H. Park, A. Camps, L. Qiao, and C. Rizos, "Detecting targets above the Earth's surface using GNSS-R delay Doppler maps: Results from TDS-1," *Remote Sens.*, vol. 11, Oct. 2019, Art. no. 2327.

[16] A. Camps and J. Munoz-Martin, "Analytical computation of the spatial resolution in GNSS-R and experimental validation at l1 and l5," *Remote Sens.*, vol. 12, Nov. 2020, Art. no. 3910.

[17] M. P. Clarizia and C. S. Ruf, "On the spatial resolution of GNSS reflectometry," *IEEE Geosci. Remote Sens. Lett.*, vol. 13, no. 8, pp. 1064–1068, Aug. 2016.

[18] A. Camps, "Spatial resolution in GNSS-R under coherent scattering," *IEEE Geosci. Remote Sens. Lett.*, vol. 17, no. 1, pp. 32–36, Jan. 2020.

[19] A. Camps and J. F. Munoz-Martin, "Analytical computation of the spatial resolution in GNSS-R and experimental validation at L1 and L5," *Remote Sens.*, vol. 12, Nov. 2020, Art. no. 3910.

[20] M. P. Clarizia and C. S. Ruf, "Bayesian wind speed estimation conditioned on significant wave height for GNSS-R ocean observations," *J. Atmos. Ocean. Technol.*, vol. 34, no. 6, pp. 1193–1202, Jun. 2017.

[21] B. Li, L. Yang, B. Zhang, D. Yang, and D. Wu, "Modeling and simulation of GNSS-R observables with effects of swell," *IEEE J. Sel. Top. Appl. Earth Obs. Remote Sens.*, vol. 13, pp. 1833–1841, 2020.

[22] J. Munoz-Martin *et al.*, "Experimental evidence of swell signatures in airborne L5/E5a GNSS-reflectometry," *Remote Sens.*, vol. 12, May 2020, p. 1759, doi: 10.3390/rs12111759.

[23] V. U. Zavorotny and A. G. Voronovich, "Scattering of GPS signals from the ocean with wind remote sensing application," *IEEE Trans. Geosci. Remote Sens.*, vol. 38, no. 2, pp. 951–964, Mar. 2000.

[24] E. Cardellach, F. Fabra, O. Nogués-Correig, S. Oliveras, S. Ribó, and A. Rius, "GNSS-R ground-based and airborne campaigns for ocean, land, ice, and snow techniques: Application to the GOLD-RTR data sets," *Radio Sci.*, vol. 46, p. RS0C04, Dec. 2011, doi: 10.1029/2011RS004683.

[25] Q. Hui and J. Shuanggen, "Global mean sea surface height estimated from spaceborne Cyclone-GNSS reflectometry," *Remote Sens.*, vol. 12, Jan. 2020, Art. no. 356.

[26] R. Stosius, G. Beyerle, A. Helm, A. Hoechner, and J. Wickert, "Simulation of space-borne tsunami detection using GNSS-reflectometry applied to tsunamis in the Indian ocean," *Natural Hazards Earth Syst. Sci.*, vol. 10, pp. 1359–1372, Jun. 2010.

[27] Q. Yan and W. Huang, "Tsunami detection and parameter estimation from GNSS-R delay-doppler map," *IEEE J. Sel. Top. Appl. Earth Obs. Remote Sens.*, vol. 9, no. 10, pp. 4650–4659, Oct. 2016.

[28] S. Lee and J. Song, "Economic possibilities of shipping though northern sea route," *Asian J. Shipping Logistics*, vol. 30, pp. 415–430, Dec. 2014.

[29] R. D. Jackson, "Soil moisture inferences from thermal-infrared measurements of vegetation temperatures," *IEEE Trans. Geosci. Remote Sens.*, vol. GE- 20, no. 3, pp. 282–286, Jul. 1982.

[30] Q. Yan, W. Huang, S. Jin, and Y. Jia, "Pan-tropical soil moisture mapping based on a three-layer model from CYGNSS GNSS-R data," *Remote Sens. Environ.*, vol. 247, 2020, Art. no. 111944.

[31] Y. H. Kerr *et al.*, "The SMOS soil moisture retrieval algorithm," *IEEE Trans. Geosci. Remote Sens.*, vol. 50, no. 5, pp. 1384–1403, May 2012.

[32] S. K. Chan *et al.*, "Assessment of the SMAP passive soil moisture product," *IEEE Trans. Geosci. Remote Sens.*, vol. 54, no. 8, pp. 4994–5007, Aug. 2016.

[33] V. Naeimi, K. Scipal, Z. Bartalis, S. Hasenauer, and W. Wagner, "An improved soil moisture retrieval algorithm for ERS and METOP scatterometer observations," *IEEE Trans. Geosci. Remote Sens.*, vol. 47, no. 7, pp. 1999–2013, Jul. 2009.

[34] S. L. Hegarat-Mascle, M. Zribi, F. Alem, A. Weisse, and C. Loumagne, "Soil moisture estimation from ERS/SAR data: Toward an operational methodology," *IEEE Trans. Geosci. Remote Sens.*, vol. 40, no. 12, pp. 2647–2658, Dec. 2002.

[35] C. Pathe, W. Wagner, D. Sabel, M. Doubkova, and J. B. Basara, "Using ENVISAT ASAR global mode data for surface soil moisture retrieval over Oklahoma, USA," *IEEE Trans. Geosci. Remote Sens.*, vol. 47, no. 2, pp. 468–480, Feb. 2009.

[36] H. Srivastava, P. Patel, Y. Sharma, and R. Navalgund, "Large-area soil moisture estimation using multi-incidence-angle RADARSAT-1 SAR data," *IEEE Trans. Geosci. Remote Sens.*, vol. 47, no. 8, pp. 2528–2535, Aug. 2009.

[37] C. C. Chew and E. E. Small, "Soil moisture sensing using spaceborne GNSS reflections: Comparison of CYGNSS reflectivity to SMAP soil moisture," *Geophys. Res. Lett.*, vol. 45, pp. 4049–4057, May 2018.

[38] A. Camps, H. Park, J. Castellví, J. Corbera, and E. Ascaso, "Single-pass soil moisture retrievals using GNSS-R: Lessons learned," *Remote Sens.*, vol. 12, Jun. 2020, Art. no. 2064.

[39] A. Alonso-Arroyo, V. U. Zavorotny, and A. Camps, "Sea ice detection using U.K. TDS-1 GNSS-R data," *IEEE Trans. Geosci. Remote Sens.*, vol. 55, no. 9, pp. 4989–5001, Sep. 2017.

[40] E. Valencia, A. Camps, N. Rodriguez-Alvarez, H. Park, and I. Ramos-Perez, "Using GNSS-R imaging of the ocean surface for oil slick detection," *IEEE J. Sel. Top. Appl. Earth Obs. Remote Sens.*, vol. 6, no. 1, pp. 217–223, Feb. 2013.

[41] M. L. Hammond *et al.*, "First assessment of geophysical sensitivities from spaceborne Galileo and BeiDou GNSS-reflectometry data collected by the U.K. TechDemoSat-1 mission," *Remote Sens.*, vol. 12, Sep. 2020, Art. no. 2927.

[42] L. Lebreton *et al.*, "Evidence that the great pacific garbage patch is rapidly accumulating plastic," *Sci. Rep.*, vol. 8, no. 1, pp. 1–15, Mar. 2018.

[43] M. Schafer, M. Strohmeier, V. Lenders, I. Martinovic, and M. Wilhelm, "Bringing up OpenSky: A large-scale ADS-B sensor network for research," in *Proc. 13th Int. Symp. Inf. Process. Sensor Netw.*, Apr. 2014, pp. 83–94.

[44] "NASA crustal dynamics data information system," 2019. [Online]. Available: https://cddis.nasa.gov/

[45] F. Hoots and R. L. Roehrich, "Models for propagation of NORAD element sets," 1980.

[46] A. Perez, J. F. Munoz-Martin, J. Querol, H. Park, and A. Camps, "Implementation of a testbed for GNSS-R payload performance evaluation," *IEEE J. Sel. Top. Appl. Earth Obs. Remote Sens.*, vol. 13, pp. 2708–2715, 2020.

[47] J. L. Garrison and S. J. Katzberg, "Detection of ocean reflected GPS signals: Theory and experiment," in *Proc. IEEE SOUTHEASTCON '97. Eng. New Century*, 1997, pp. 290–294.

[48] H. Park, A. Camps, J. Castellvi, and J. Muro, "Generic performance simulator of spaceborne GNSS-reflectometer for land applications," *IEEE J. Sel. Top. Appl. Earth Obs. Remote Sens.*, vol. 13, pp. 3179–3191, 2020.

[49] M. J. Brodzik, B. Billingsley, T. Haran, B. Raup, and M. H. Savoie, "EASE-Grid 2.0: Incremental but significant improvements for earth-gridded data sets," *ISPRS Int. J. Geo-Inform.*, vol. 1, no. 1, pp. 32–45, 2012.

[50] H. Carreno-Luengo, G. Luzi, and M. Crosetto, "Above-ground biomass retrieval over tropical forests: A novel GNSS-R approach with CyGNSS," *Remote Sens.*, vol. 12, no. 9, 2020, Art. no. 1368.

[51] J. Räisänen and J. Eklund, "21st century changes in snow climate in northern Europe: A high-resolution view from ENSEMBLES regional climate models," *Climate Dyn.*, vol. 38, pp. 2575–2591, Apr. 2011.

[52] S. Quegan et al., "The European space agency BIOMASS mission: Measuring forest above-ground biomass from space," *Remote Sens. Environ.*, vol. 227, pp. 44–60, Jun. 2019.

[53] J. F. Munoz-Martin et al., "Single-pass soil moisture retrieval using GNSS-R at L1 and L5 bands: Results from airborne experiment," *Remote Sens.*, vol. 13, Feb. 2021, Art. no. 797.

[54] H. Carreno-Luengo, G. Luzi, and M. Crosetto, "First evaluation of topography on GNSS-R: An empirical study based on a digital elevation model," *Remote Sens.*, vol. 11, no. 21, 2019, Art. no. 2556.

[55] F. Martin et al., "Mitigation of direct signal cross-talk and study of the coherent component in GNSS-R," *IEEE Geosci. Remote Sens. Lett.*, vol. 12, no. 2, pp. 279–283, Feb. 2015.

[56] J. Querol, A. Alonso-Arroyo, R. Onrubia, D. Pascual, H. Park, and A. Camps, "SNR degradation in GNSS-R measurements under the effects of radio-frequency interference," *IEEE J. Sel. Top. Appl. Earth Obs. Remote Sens.*, vol. 9, no. 10, pp. 4865–4878, Oct. 2016.

[57] R. Onrubia, J. Querol, D. Pascual, A. Alonso-Arroyo, H. Park, and A. Camps, "DME/TACAN impact analysis on GNSS reflectometry," *IEEE J. Sel. Top. Appl. Earth Obs. Remote Sens.*, vol. 9, no. 10, pp. 4611–4620, Oct. 2016.

[58] R. Oliva et al., "SMOS radio frequency interference scenario: Status and actions taken to improve the RFI environment in the 1400-1427 MHz passive band," *IEEE Trans. Geosci. Remote Sens.*, vol. 50, no. 5, pp. 1427–1439, May 2012.

[59] P. Richaume et al., "RFI in SMOS measurements: Update on detection, localization, mitigation techniques and preliminary quantified impacts on soil moisture products," in *Proc. IEEE Geosci. Remote Sens. Symp.*, Jul. 2014, pp. 223–226.

[60] N. Rodriguez-Alvarez, D. M. Akos, V. U. Zavorotny, J. A. Smith, A. Camps, and C. W. Fairall, "Airborne GNSS-R wind retrievals using delay-doppler maps," *IEEE Trans. Geosci. Remote Sens.*, vol. 51, no. 1, pp. 626–641, Jan. 2013.

[61] E. Valencia, V. U. Zavorotny, D. M. Akos, and A. Camps, "Using DDM asymmetry metrics for wind direction retrieval from GPS ocean-scattered signals in airborne experiments," *IEEE Trans. Geosci. Remote Sens.*, vol. 52, no. 7, pp. 3924–3936, Jul. 2014.

[62] NASA, "NASA, New Zealand partner to collect climate data from commercial aircraft," Feb. 2020. [Online]. Available: https://www.nasa.gov/feature/goddard/2020/nasa-new-zealand-partner-to-collect-climate-data-from-commercial-aircraft
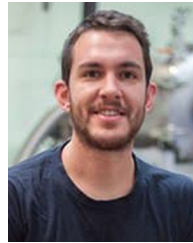
Adrian Perez-Portero was born in Barcelona, Spain, in 1992. He received the M.Sc. degree in telecommunications engineering from the Universitat Politecnica de Catalunya—UPC BarcelonaTech, Barcelona, Spain. He is currently working toward the Ph.D. degree in the field of radio frequency interference and signal processing.

He joined the NanoSat-Lab, Barcelona, Spain, in 2018 as a Software Engineer, working on several projects related to GNSS technologies such as RFI mitigation and GNSS-R simulation. He is currently participating in the ³Cat-4 and ESA S³ FSSCat mission as Software, Ground Segment and Operations Engineer. He is also currently working on the FENIX (Front-End GNSS Interference eXcisor) and other RFI detection products, as well as in the RITA payload.

Mr. Perez-Portero leads the winner team of the 2nd GRSS Student Challenge.

Joan Francesc Munoz-Martin (Member, IEEE) was born in Mallorca, Spain, in 1992. He received the M.Sc. degree in telecommunications engineering from the Universitat Politecnica de Catalunya, Barcelona, Spain. He is currently working toward the Ph.D. degree.

He joined the NanoSat Lab, Barcelona, Spain, in 2013 as a Communications System Engineer for the 3Cat-1 mission and has been involved in all its missions ever since. He participated in ESA's BEXUS 19 and led the OBDH, TT&C, and Ground Operations for 3Cat-2 mission. As part of his doctoral degree, he participated in 3Cat-4 and ESA S³ FSSCat mission. He is the Lead Software and Payload Engineer for the FMPL-1, and the Payload Manager of FMPL-2, the GNSS-R, and radiometry microwave passive payloads of 3Cat-4 and FSSCat, respectively. He is also part of the science team of the GNSS-R experiment carried out in the MOSAiC campaign in the Arctic sea.

Hyuk Park (Senior Member, IEEE) was born in South Korea. He received the B.S. degree in mechanical engineering from the Korea Advanced Institute of Science and Technology (KAIST), Daejeon, South Korea, in 2001, and the M.S. and Ph.D. degrees in information and mechatronics from the Gwangju Institute of Science and Technology (GIST), Gwangju, South Korea, in 2003 and 2009, respectively.

He joined the remote sensing group of the Polytechnic University of Catalonia (UPC), Barcelona, Spain, as a Postdoctoral Researcher in 2009. In 2012–2014, he has worked as a Juan de la Cierva Researcher funded by Spanish Ministry of Science and Innovation. He is currently working with School of Telecommunications and Aerospace Engineering, RSLab, Universitat Politècnica de Catalunya as a Ramon y Cajal Fellow/Tenure-Track Assistant Professor. His main research interests are in the areas of remote sensing, especially passive microwave remote sensing, including system design, modeling and simulation, and image processing.

Dr. Park is a grant holder of NRF funded by the Korean government in 2011.

Adriano Camps (Fellow, IEEE) was born in Barcelona, Spain, in 1969. In 1992, he received the "ingeniero" (bachelor + M.Eng.) degree in telecommunications engineering and in 1996, the Ph.D. degree in telecommunications engineering from the Universitat Politècnica de Catalunya (UPC), Barcelona, Spain.

He was with the ENS des Télécommunications de Bretagne, Brest, France, with an Erasmus Fellowship from 1991 to 1992. Since 1993, he has been with the Electromagnetics and Photonics Engineering Group, Department of Signal Theory and Communications, UPC, where he was first an Assistant Professor, an Associate Professor in 1997, and a Full Professor since 2007. In 1999, he was on sabbatical leave at the Microwave Remote Sensing Laboratory, University of Massachusetts, Amherst, MA, USA. Since 1993, he has been deeply involved in the European Space Agency SMOS Earth Explorer Mission, from the instrument and algorithmic points of view, performing field experiments, and since 2001, studying the use of GNSS-R techniques to perform the sea state correction needed to retrieve salinity from L-band radiometric observations. His research interests are focused in microwave remote sensing, with special emphasis in microwave radiometry by aperture synthesis techniques, remote sensing using signals of opportunity (GNSS-R), radio-frequency detection, and mitigation techniques for microwave radiometry and GNSS, and CubeSats as platforms to test novel remote sensing concepts. He has authored or coauthored more than 216 papers in peer-reviewed journals, 6 book chapters, 1 book, and more than 450 international conference presentations, holds 12 patents, and has advised 25 Ph.D. Thesis students (+8 on-going), and more than 140 final projects and M.Eng. theses. According to Publish or Perish (Google Scholar), his publications have received more than 7161/10706 citations, and his h-index is 39/51 according to Scopus/Google Scholar.

Prof. Camps was the IEEE GRSS President from 2017 to 2018, Technical Program Committee Chair of IGARSS 2017, General Cochair of IGARSS 2020, and has been involved in the organization of several other conferences. He is also the recipient of several awards including the EURopean Young Investigator (EURYI) Award 2004, the Duran Farell Award for technology transfer in 2000 and 2010, the ICREA Acadèmia Research Award in 2008 and 2014 etc.